Document Version
Final published version

Licence
CC BY

Citation (APA)
Johannsen, P. D., Legg, H. F., Bosco, S., Loss, D., & Klinovaja, J. (2026). Atypical Josephson effect in hybrid superconductor-hole systems. *Physical Review Research*, *8*(1), Article 013289. https://doi.org/10.1103/dqgc-8crs

PRX QUANTUM **7,** 010308 (2026)

Featured in Physics

Running a Six-Qubit Quantum Circuit on a Silicon Spin-Qubit Array

I. Fernández de Fuentes,[1,*,†] E. Raymenants,[1,*] B. Undseth,[1] O. Pietx-Casas,[1] S. Philips,[1]
M. Mądzik,[1] S.L. de Snoo,[1] S.V. Amitonov,[2] L. Tryputen,[2] A.T. Schmitz,[3] A.Y. Matsuura,[3]
G. Scappucci,[1] and L.M.K. Vandersypen[1]

[1] *QuTech and Kavli Institute of Nanoscience, Delft University of Technology, Lorentzweg 1, 2628 CJ Delft, The Netherlands*
[2] *QuTech and Netherlands Organization for Applied Scientific Research (TNO), Delft, The Netherlands*
[3] *Intel Corporation, Hillsboro, Oregon 97124, USA*

(Received 25 May 2025; revised 18 September 2025; accepted 13 November 2025; published 14 January 2026)

The simplicity of encoding a qubit in the state of a single electron spin and the potential for their integration into industry-standard microchips continue to drive the field of semiconductor-based quantum computing. After a series of key first-principles demonstrations validating universal gate operations, initialization and readout, three-qubit algorithms have already been realized with silicon-based quantum dots in past years. Devices containing more qubits have become available since then but experiments have not gone beyond meeting the DiVincenzo criteria. In this work, we fully exploit the capacity of a spin-qubit array and implement a six-qubit quantum circuit, the largest utilizing semiconductor quantum technology. By programming the quantum processor, we execute quantum circuits across all permutations of three, four, five, and six neighboring qubits, demonstrating successful programmable multi-qubit operation throughout the array. Using an error model that incorporates quasi-static noise allows us to qualitatively explain some key trends in our experimental results and highlight the necessity to minimize idling times through simultaneous operations, extending dephasing times, and consistently improving state preparation and measurement fidelities.

DOI: 10.1103/f285-l2v5

I. INTRODUCTION

The prospect of achieving quantum advantage and real-world applications drives the rapidly evolving field of quantum technologies. For quantum computing, a major challenge in outpacing classical devices is scaling the number of qubits while maintaining high-fidelity initialization, control, and readout of the qubits.

Over the past decades, platforms based on superconducting qubits [1], neutral atoms [2] and trapped ions [3,4] have come forward increasing the number and quality of qubits, enabling important milestones such as the first demonstrations of logical encoding for quantum error correction [1,4,5] or experimental studies of many-body phenomena [6–8].

Following in their steps, quantum hardware based on semiconductor spin qubits is raising the stakes by leveraging industry-standard fabrication techniques to scale up [9–14]. Considerable focus has been given to validate these platforms by demonstrating and refining high-fidelity single- [15] and two-qubit gates [16–18], as well as initialization and readout [15,19,20]. This progress has enabled the execution of realistic quantum circuits with two [21], three [22–24] and four qubits [25,26]. In an array of ten quantum dots, single-qubit operations were characterized one at a time [27]. Finally, in a six-qubit device, initialization, single- and two-qubit gates, and readout were simultaneously tuned up across the full system, although entangling circuits were implemented with up to three qubits only [28].

In this work, we go a step further and assess the performance of a six-qubit array when all the available units in the quantum processor are involved in the quantum circuit. This is a crucial aspect, as a potential bottleneck for the scalability of these noisy intermediate-scale devices arises precisely from this collective operation: as more units are added, errors accumulate, overall processor operation slows down, and the available coherence budget for quantum operations becomes limiting.

---

[*] These authors contributed equally to this work.
[†] Contact author: ifernandezdefu@tudelft.nl

We utilize six single-spin qubits arranged in a linear array of quantum dots to run a multi-qubit quantum circuit inspired by a protocol designed to investigate dynamical quantum phase transitions in Ising-like systems. Leveraging single-qubit control through addressable microwave driving and tunable two-qubit exchange interactions, we showcase the quantum processor's programmability in operating with any combination of three, four, five, or six qubits. To demonstrate and validate this capability, we employ a protocol that can flexibly accommodate an increasing number of qubits with a well-understood expected scaling of its output. This enables us to identify key bottlenecks observed in our device particularly with regard to idling and runtime, as well as state preparation and measurement (SPAM) errors, while also outlining potential pathways for improvement that are expected to be relevant across similar platforms.

This manuscript is organized as follows. In Sec. II we present details on the quantum processor platform and its operation. The implemented quantum circuit is described in Sec. III. In Sec. IV A we report the experimental results obtained from running the quantum circuit and discuss the sources of error which limit the performance of the quantum processor. We provide further benchmarks through quantum state tomography (QST) in Sec. IV B. Finally, we discuss the implications of the results in Sec. V.

II. DEVICE, INITIALIZATION AND READOUT

The six electron spin qubits are hosted in an array of six quantum dots that are electrostatically defined within a ^{28}Si/SiGe heterostructure. The dots are formed below the plunger gates of the device depicted in Fig. 1(a). Details on the design, operation and calibration of the system are extensively covered in Ref. [28]. However, we revisit and extend the readout and initialization schemes as they must be adapted for the experiments here. Additionally, we intentionally operate the device at 200 mK to reduce unwanted heating effects induced by the delivery of microwave signals during qubit control [29].

The initialization and readout sequences are depicted in the blue- and gray-shaded areas in Fig. 1(a), respectively. For compactness, the steps for qubits 1–3 and for qubits 4–6 are illustrated as occurring simultaneously in the diagram, but in practice they are executed sequentially.

Readout relies on two charge-sensing dots, one on each end of the array and labeled as "SD" in the false-colored scanning electron microscope image. Each sensing dot is used for reading out the spin state of the two nearest confined electrons, namely pair 1-2 and pair 5-6, through parity-mode Pauli Spin Blockade (PSB) [30] (see Appendix). Note that throughout the text, we may occasionally refer to "parity-mode PSB" as simply "PSB." The associated measurement operator $\mathcal{M}_{ZZ} = (1 + ZZ)/2$, returns a 0 or a 1 depending on whether the spins are in an antiparallel (odd) or parallel (even) configuration, respectively. Due to the specifics of the PSB readout used here, the postmeasurement state for an odd parity outcome will be the $|\uparrow\downarrow\rangle$ ($|\downarrow\uparrow\rangle$) state with high probability for qubits 1-2 (5-6), regardless of the premeasurement state (see Appendix). For the even parity outcomes, the postmeasurement state with high probability is the same as the premeasurement state.

As charge sensing is less efficient for the inner dots due to their greater distance from the sensing dots, the spin state of qubit 3 (4) is read out via a quantum nondemolition (QND) measurement [31] whereby the state of qubit 3 (4) is mapped onto that of qubit 2 (5) by a conditional $X(\pi)$-rotation, which can be subsequently measured via PSB as shown in Fig. 1(b). With a reference parity measurement, we can use the probability of parity flipping as a proxy for the measurement operator $\mathcal{M}_Z = (1 + Z)/2$ on qubits 3 and 4, as illustrated in the truth table in Fig. 1(c). Furthermore, the QND measurement procedure can be repeated to boost the measurement fidelity by taking a majority vote of repeated measurements.

Applying the parity measurement protocol to qubits 1-2 and 5-6 and the QND measurement protocol to qubits 3 and 4 within a single measurement cycle yields 4 bits of information regarding the state of the full array provided by the measurement operators $\mathcal{M}_{Z_1Z_2}$,$\mathcal{M}_{Z_3}$, $\mathcal{M}_{Z_4}$ and $\mathcal{M}_{Z_5Z_6}$ [28].

For the successful implementation of the quantum circuit, as will be detailed in Sec. III, an extended readout scheme is necessary to obtain the so-called *return probability*. This probability is defined as the overlap of the initial and final quantum states, $|\langle\psi_0|\,|\psi_f\rangle|^2$. Specifically, we aim at initializing and measuring the return probability of the $|\psi_0\rangle = |\downarrow\rangle^{\otimes N}$ state, with N being the number of qubits. However, in the current PSB readout scheme for qubit pairs 1-2 and 5-6 [28], it is inherently not possible to discriminate between $|\downarrow\downarrow\rangle$ and $|\uparrow\uparrow\rangle$ and also not between $|\uparrow\downarrow\rangle$ and $|\downarrow\uparrow\rangle$. As a result, the return probability to the $|\downarrow\rangle^{\otimes N}$ state cannot be directly measured.

To overcome this limitation, two-qubit logic can be employed to isolate the $|\downarrow\rangle^{\otimes N}$ state from all the other states. This approach is illustrated in the circuit schematics from Fig. 1(d). The scheme begins with a first measurement $\mathcal{M}^{\mathrm{C}}_{ZZ}$, which determines if the spin parity of qubit pair 1-2 is even or odd (the scheme for qubit pair 5-6 is analogous). Next, a controlled-NOT (CNOT) gate is applied between the parity pairs using qubit 2 as the control qubit and qubit 1 as the target qubit.

We compile the CNOT using a sequence of operations which leverages the native two-qubit ZZ interaction as shown schematically in Fig. 1(e) (see Appendix). A second parity measurement $\mathcal{M}^{\mathrm{D}}_{ZZ}$ follows the CNOT operation, leading to the possible outcomes listed in Fig. 1(f). By selecting outcomes where the parity is even in both $\mathcal{M}^{\mathrm{C}}_{ZZ}$ and $\mathcal{M}^{\mathrm{D}}_{ZZ}$, the state $|\downarrow\downarrow\rangle$ can be isolated resulting

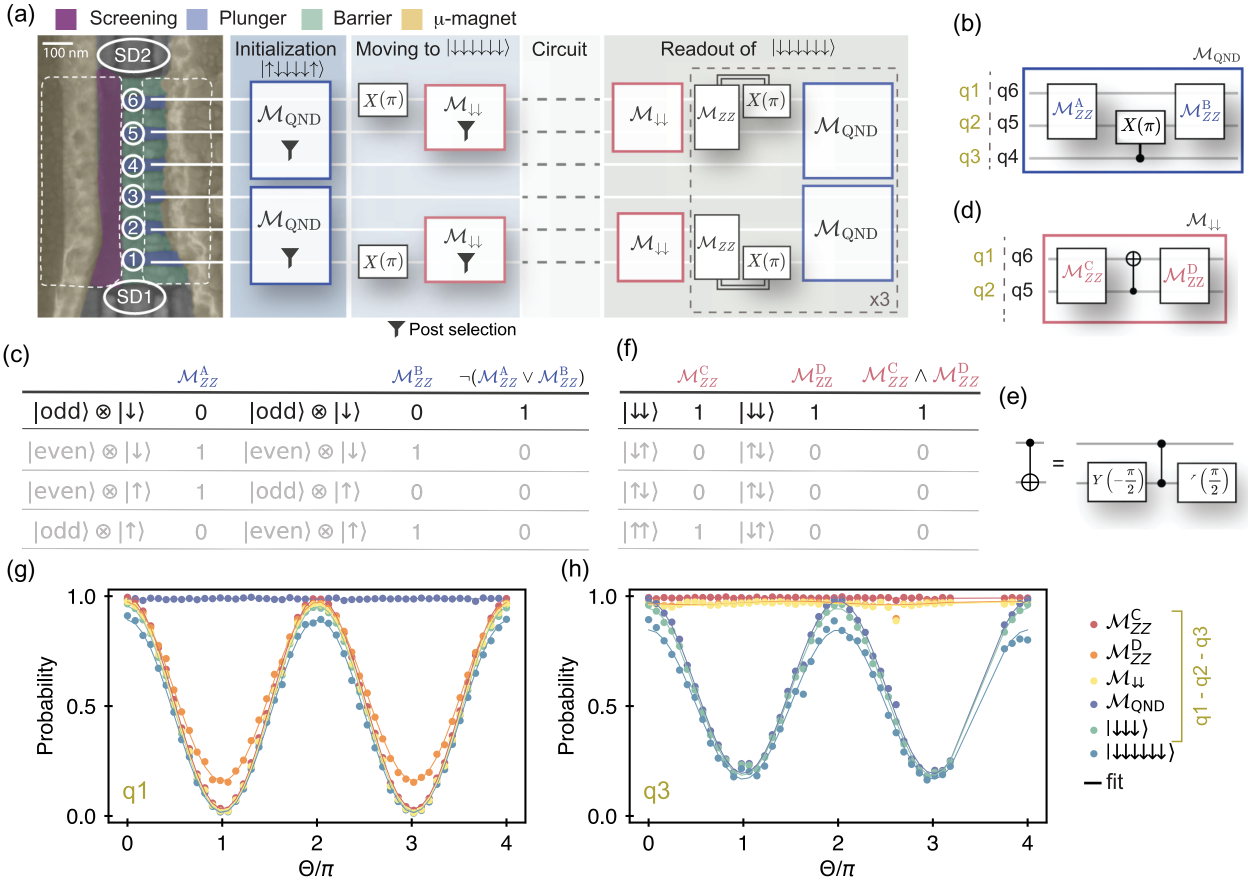

(c)

	$\mathcal{M}_{ZZ}^{\mathrm{A}}$		$\mathcal{M}_{ZZ}^{\mathrm{B}}$	$\neg(\mathcal{M}_{ZZ}^{\mathrm{A}} \vee \mathcal{M}_{ZZ}^{\mathrm{B}})$
$\|\mathrm{odd}\rangle \otimes \|\downarrow\rangle$	0	$\|\mathrm{odd}\rangle \otimes \|\downarrow\rangle$	0	1
$\|\mathrm{even}\rangle \otimes \|\downarrow\rangle$	1	$\|\mathrm{even}\rangle \otimes \|\downarrow\rangle$	1	0
$\|\mathrm{even}\rangle \otimes \|\uparrow\rangle$	1	$\|\mathrm{odd}\rangle \otimes \|\uparrow\rangle$	0	0
$\|\mathrm{odd}\rangle \otimes \|\uparrow\rangle$	0	$\|\mathrm{even}\rangle \otimes \|\uparrow\rangle$	1	0

(f)

	$\mathcal{M}_{ZZ}^{\mathrm{C}}$		$\mathcal{M}_{ZZ}^{\mathrm{D}}$	$\mathcal{M}_{ZZ}^{\mathrm{C}} \wedge \mathcal{M}_{ZZ}^{\mathrm{D}}$
$\|\downarrow\downarrow\rangle$	1	$\|\downarrow\downarrow\rangle$	1	1
$\|\downarrow\uparrow\rangle$	0	$\|\uparrow\downarrow\rangle$	0	0
$\|\uparrow\downarrow\rangle$	0	$\|\uparrow\downarrow\rangle$	0	0
$\|\uparrow\uparrow\rangle$	1	$\|\downarrow\uparrow\rangle$	0	0

FIG. 1. Device initialization and readout scheme. (a) False-colored scanning electron microscope image of a device nominally identical to the one used, alongside the quantum circuit schematic for initializing and reading out all six qubits. Electrons are confined in quantum dots centered beneath the plunger gates and in between two screening gates (white-dashed contours). The interdot tunnel coupling is controlled via the barrier gates. The cobalt micromagnet deposited on top creates a magnetic field gradient enabling single-qubit addressability while also producing synthetic spin–orbit coupling for single-spin control via electric-dipole spin resonance by driving a screening gate. (b) Quantum circuit used to construct the measurement operator $\mathcal{M}_{\mathrm{QND}}$ by means of a quantum nondemolition measurement. (c) The corresponding truth table based on the parity measurements $\mathcal{M}_{ZZ}^{\mathrm{A}}$ and $\mathcal{M}_{ZZ}^{\mathrm{B}}$. Highlighted is the state that we postselect after measurement for initialization based on the operator $\mathcal{M}_{Z}^{\mathrm{QND}}$ which is extracted as shown in the last column. (d) Quantum circuit to build the operator $\mathcal{M}_{\downarrow\downarrow}$. Here, the parity measurements $\mathcal{M}_{ZZ}^{\mathrm{C}}$ and $\mathcal{M}_{ZZ}^{\mathrm{D}}$ allow discrimination of the $|\downarrow\downarrow\rangle$ state using the truth table in (f), corresponding to two even outcomes. (e) Compilation of the CNOT gate used in (d). (f) Truth table for the parity readouts $\mathcal{M}_{ZZ}^{\mathrm{C}}$ and $\mathcal{M}_{ZZ}^{\mathrm{D}}$. The notation here assumes that the arrows in the ket correspond to qubits 1 or 6 for the first arrow and qubits 2 or 5 for the second. Note that the state $|\downarrow\uparrow\rangle$ decays to the $|\uparrow\downarrow\rangle$ after the first Pauli Spin Blockade. Highlighted is the state that we postselect after measurement for initialization. The operator $\mathcal{M}_{ZZ}^{\downarrow\downarrow}$ is extracted through the logical combination shown in the last column. (g) and (h) Rabi experiments obtained for qubits 1 and 3 after preparing the array in the $|\downarrow\rangle^{\otimes 6}$ state and applying a resonant drive to achieve a calibrated rotation of an angle θ of (g) qubit 1 and (h) qubit 3. The various data points (see legend) show all intermediate observables as well as the probability for obtaining $|\downarrow\rangle^{\otimes 3}$ in the subspace 1-2-3 and the return probability to the $|\downarrow\rangle^{\otimes 6}$ state. The solid lines correspond to fits using sinusoidal functions.

in an effective measurement of the observable $\mathcal{M}_{\downarrow\downarrow} = |\downarrow\downarrow\rangle\langle\downarrow\downarrow|$ for the first two and the last two qubits. As before, measurement of qubits 3 and 4 is implemented directly through $\mathcal{M}_{\mathrm{QND}}$. While not strictly necessary, we incorporate an additional step within the readout sequence, marked by the rotation of qubits 1 and 6 conditional on an even parity outcome, which takes the pairs to the lower-energy antiparallel configuration before $\mathcal{M}_{\mathrm{QND}}$ readout. This approach is motivated by the fact that it yields a higher number of retained traces after the initialization sequence of the next round, since we initialize odd states, as will be explained next.

We prepare the qubits using initialization by measurement and postselection, making use of similar sequences as during readout [light and dark blue region in Fig. 1(a)]. First, we perform a QND measurement on qubits 3 and 4 and postselect for $|\downarrow\rangle$ outcomes for these qubits and for odd outcomes on qubits 1-2 and 5-6 during $\mathcal{M}_{ZZ}^{\mathrm{B}}$

readout. This results in the postselected postmeasurement state $|\uparrow\downarrow\downarrow\downarrow\downarrow\uparrow\rangle$ [28]. After flipping qubits 1 and 6 with a resonant π-pulse, the $|\downarrow\downarrow\downarrow\downarrow\downarrow\downarrow\rangle$ state is prepared. While not strictly necessary, we add another set of parity measurements to confirm the outer qubit pairs are set to $|\downarrow\downarrow\rangle$. Unless stated otherwise, we prepare and measure all six qubits in all the experiments, even when not all qubits are involved in the circuit, to ensure that SPAM errors are similar. Additionally, systematic sensor drifts from residual microwave heating are mitigated during postprocessing (Supplemental Material S1 [32]).

To validate the extended initialization and readout scheme, we resonantly drive Rabi oscillations on individual qubits using electric-dipole spin resonance and inspect the probability of measuring individual and composite observables. The results for driving qubits 1 or 3 are depicted in Figs. 1(g) and 1(h) as an example, and the same experiments for all six qubits can be found in Supplemental Material S2 [32]. Looking at the experimental results in Fig. 1(g), we observe oscillations in the $\mathcal{M}_{\downarrow\downarrow}$ and $|\downarrow\rangle^{\otimes 3}$ probabilities while the $\mathcal{M}_{\text{QND}}$ probability stays constant, which is consistent with coherently driving qubit 1 only. Analogously, the data in Fig. 1(h) shows that $\mathcal{M}_{ZZ}^{\text{C}}$, $\mathcal{M}_{ZZ}^{\text{D}}$ and consequently $\mathcal{M}_{\downarrow\downarrow}$ remain flat, while $\mathcal{M}_{\text{QND}}$ oscillates, verifying that the oscillations in the $|\downarrow\rangle^{\otimes 3}$ probability are purely due to changes in the state of qubit 3. In both cases, also the $|\downarrow\rangle^{\otimes 6}$ probability oscillates, as expected. In interpreting the data, it is good to keep in mind that the AND logic between the outcomes of $\mathcal{M}_{ZZ}^{\text{C}}$ and $\mathcal{M}_{ZZ}^{\text{D}}$ inherently biases the results toward lower values in the presence of SPAM errors (see Supplemental Material S3 [32] for a rigorous derivation). We also highlight that the addition of two-qubit gates reduces the Rabi oscillation visibility, as observed by comparing the outcomes of $\mathcal{M}_{ZZ}^{\text{C}}$ and $\mathcal{M}_{ZZ}^{\text{D}}$. We expect a similar effect in the QND measurement. To avoid overcrowding the figures, we do not show the intermediate readouts on the other half of the array in Figs. 1(g) and 1(h). Naturally, a reduction in the oscillation amplitude of the probability to return to the $|\downarrow\rangle^{\otimes 6}$ is expected when combining the readout measurements from qubits 4, 5, and 6 from accumulated SPAM errors decreasing the visibility by approximately 6% for qubit 1 and 10% for qubit 3.

III. QUANTUM CIRCUIT DESCRIPTION

Having established the initialization and readout procedure, we now turn to detailing the quantum circuit used in this work. The circuit in Fig. 2(a) depicts a digital protocol where a quantum state described by the ground state of an initial Hamiltonian $H_0 = h\sum_{i=1}^{N} Z_i$ undergoes a quantum quench by suddenly activating the interaction Hamiltonian $H_{\text{quench}}(h=0) = J_0\left[\sum_{i=1}^{N-1} X_iX_{i+1} + X_1 + X_N\right]$. Here, h denotes the strength of the on-site longitudinal field, while J_0 governs both the strength of the nearest-neighbor coupling and the boundary conditions via the edge terms X_1 and X_N (see Supplemental Material S4 A [32]). The corresponding out-of-equilibrium dynamics can be effectively mapped to a circuit composed of single- and two-qubit gates as displayed, without the need of Trotterization. Note that we do not need to implement the second set of CNOT gates in Fig. 2(b) because the experiments are focused on the case where the initial state $|\psi_0\rangle = |\downarrow\rangle^{\otimes N}$, the ground state of H_0. In this scenario, the evolution under the XX interactions can be simplified to the circuit in Fig. 2(a). A detailed derivation for the mapping of the quenching Hamiltonian and the aforementioned simplification can be found in Supplemental Material S4 B [32]. Our motivation to choose this particular protocol stems from its simplicity while still incorporating both single-qubit operations on all qubits and two-qubit interactions between all neighboring qubits in a linear chain. Furthermore, in the course of the circuit execution, all qubits are expected to become entangled. This scheme thus constitutes a meaningful first test of the full six-qubit device under a workload which leverages the device's native connectivity.

Figure 2(a) illustrates the circuit when all six qubits in the array are used. The adaptation of the quantum circuit for $N = \{3, 4, 5\}$ is achieved by omitting one, two, or three of the inner circuit channels, respectively. Time evolution is parameterized by the angle θ, which we can experimentally vary by sweeping the duration t_{MW} of a microwave burst on resonance with the target qubit, such that $\theta = \pi\, t_{\text{MW}}/t_\pi$ with t_π being the time needed to perform a full flip of the spin, ranging from 94 to 250 ns. Entanglement is distributed across the array via the CNOT gates, compiled as shown in the schematic of Fig. 2(c) with a typical duration of 100–800 ns.

As introduced in Sec. II, in these experiments we are interested in tracking the overlap of the initial state $|\psi_0\rangle$ with a final state–the time-evolved state $|\psi(t)\rangle$ in this case–referred to as the return probability. This metric, also known as the Loschmidt echo amplitude, is commonly used to probe the complex dynamics of interacting quantum systems [33,34], and it is formally defined as $\mathcal{L}(\theta) = |\langle\psi_0|\,|\psi(\theta)\rangle|^2 = |\langle\psi_0|\, e^{-iHt}\,|\psi_0\rangle|^2$. The chosen protocol compares with models which have been previously studied in the context of dynamical quantum phase transitions (DQPTs) [33,35]. While our aim is not to focus on the physical implications within the framework of quantum phase transitions, we want to draw attention to the scaling of the Loschmidt echo amplitude when the number of qubits, N, involved in the dynamics change, which can be expressed analytically as (see Supplemental Sec. S4 C [32])

$$\mathcal{L}(\theta) = \left|\cos\left(\frac{\theta}{2}\right)^{N+1} + i^{N+1}\sin\left(\frac{\theta}{2}\right)^{N+1}\right|^2. \quad (1)$$

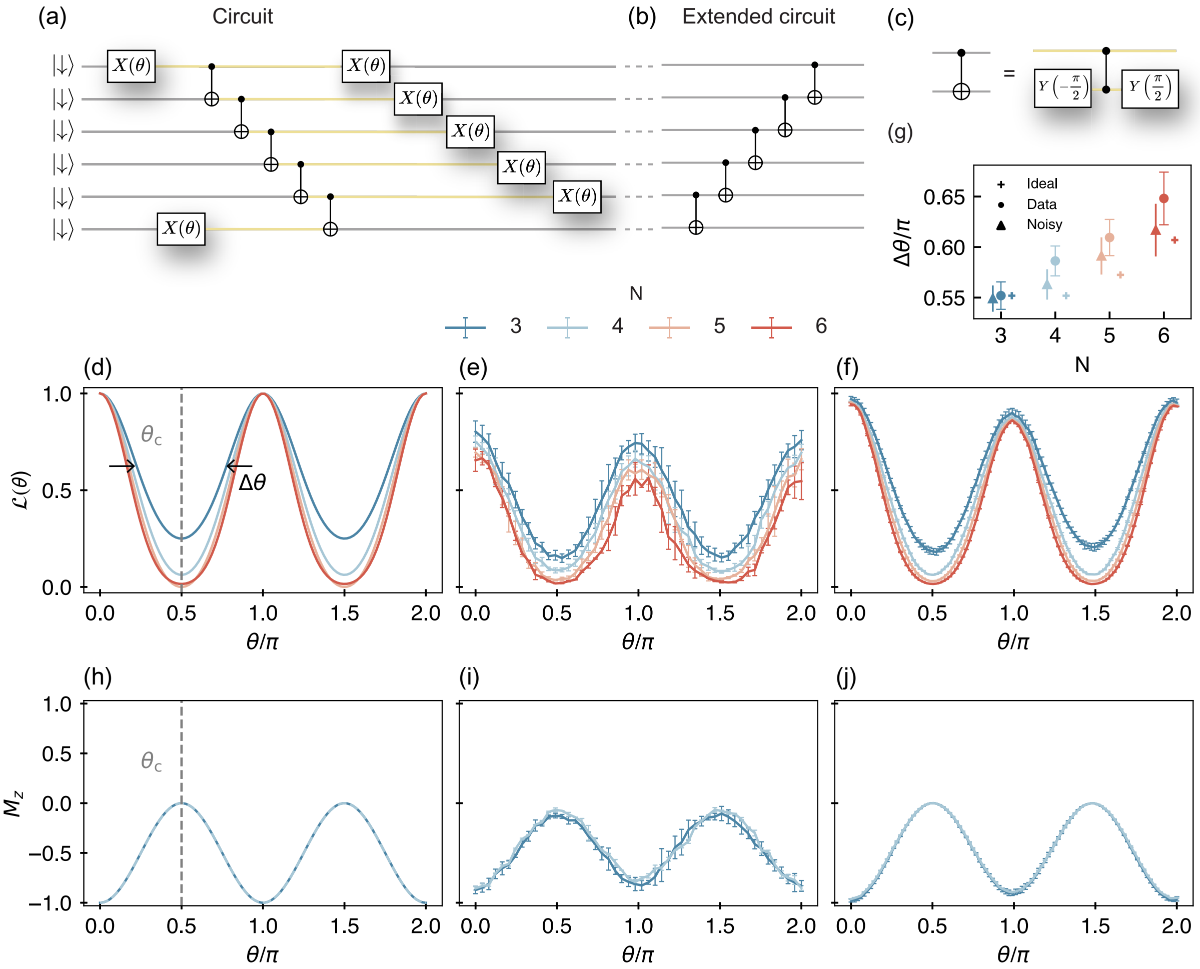

FIG. 2. Quantum circuit diagram and results. (a) Quantum circuit diagram to perform a quantum quench. This circuit is to be executed in between initialization of the system in $|\downarrow\downarrow\downarrow\downarrow\downarrow\downarrow\rangle$ and the measurement of the return probability, shown in Fig. 1(a). The yellow coloring highlights idle periods of the qubits between gate operations, also shown for (c). (b) Quantum circuit extension needed for the initial-state-independent version of the circuit. (c) Quantum circuit showing how the CNOT operations in (a) are compiled. (d)–(f) Return probability $\mathcal{L}$ as a function of θ obtained from (d) a numerical simulation not accounting for noise, (e) experiments, for each N averaged over all possible permutations of neighboring qubits, and (f) numerical simulations including dephasing errors from quasi-static noise. (g) Broadening of the curves $\Delta\theta$ as a function of system size N for panels (d) (*ideal*), (e) (*data*) and (f) (*noisy*), quantified using the methodology described in Appendix. For readability, we have added a small offset to the x-values of the different datasets plotted in the same figure. Error bars are calculated using one standard deviation. (h)–(j) Magnetization defined as $M_z = \frac{1}{N}\sum_i^N Z_i$ for N is 3 or 4, obtained from (h) a numerical simulation not accounting for noise, (i) experiments, for each N averaged over all possible permutations of neighboring qubits among qubits 2, 3, 4 and 5, and (j) numerical simulations including dephasing errors from quasi-static noise. The error bars in the experimental panels correspond to one standard deviation.

From Eq. (1), we observe that the Loschmidt echo amplitude exhibits a periodicity of $\theta = \pi$ and depends on N. Figure 2(d) illustrates the expected $\mathcal{L}(\theta)$ for N varying from three to six. As N increases, the Loschmidt echo exhibits a broader and deeper minimum, indicating that $|\psi(\theta)\rangle$ evolves faster and farther away from the initial $|\psi_0\rangle$. In all cases, $\mathcal{L}(\theta)$ reaches a minimum at $\theta = \pi/2$, referred to as the *critical time* θ_c in the DQPT terminology. An analogy to equilibrium statistical physics is often drawn for these critical points, particularly relating them to phase transitions in which thermodynamical properties become nonanalytical (see Supplemental Material S4 C [32] for details). Lastly, we want to highlight that the periodicity observed in Fig. 2(d) differs from what one would expect from a periodicity of 2π based solely on single-qubit rotations, $X(\theta)$. The two-qubit interactions are responsible for the periodicity of $\theta = \pi$ (see Supplemental Material S5 [32] for more detail).

IV. EXPERIMENTAL RESULTS

A. Measurements of return probability and magnetization

Using the methodology for state preparation and measurement described in Sec. II, we run the quantum circuit presented in Fig. 2(a) for different system sizes, $N \in \{3, 4, 5, 6\}$. We note that the operations are performed sequentially in the current implementation of the circuit, as illustrated in Fig. 2(a) by appending the gates in the circuit. The experimental results are presented in Fig. 2(e), featuring the Loschmidt echo amplitude as a function of angle θ and number of particles N. Importantly, these datasets were collected on the same day after a full calibration round as described in Subsection 3 in Appendix.

Each trace in Fig. 2(e) displays the average result after executing the circuit across all possible qubit combinations for varying system sizes. For instance, for $N = 5$, we average over four datasets, involving either qubits 1–5 or qubits 2–6, and with the five retained qubits ordered sequentially or in reverse. Acknowledging that individual qubit combinations may exhibit varying performance, we use this approach as an estimation of the *average behavior* of the quantum processor. The separate measurement results for all cases are presented in Fig. S5 of the Supplemental Material [32]. There, we also include the raw data for which the readout signal was not re-thresholded to mitigate sensor drifts due to heating. The results feature the oscillations as a function of angle θ, as predicted by Eq. (1), showing that the quantum state evolves periodically through regions of maximum and minimum overlap with the initial state with period $\theta = \pi$ and critical angle $\theta_c = \pi/2$. As previously discussed, this indicates that interactions across the entirety of the array can indeed be controllably activated to realize successive two-qubit gates. We can also appreciate that increasing N results in broader dips, consistent with predictions. Using the procedure described in Appendix, we quantify this broadening through the width $\Delta\theta$, and plot in Fig. 2(c) its dependence on N for the ideal case, the experimental data and the simulations with quasi-static noise.

Despite the overall similarities between theory and experiment, it is noticeable that the experiments feature an N-dependent offset of the curves at $\theta = 0$ and overall loss of visibility. In addition, we observe a decay increasing with θ especially for larger N. The N-dependent offset is not likely a consequence of SPAM errors accumulating as N increases, as all qubits are prepared and read out independent of the number of qubits that are used in the circuit. However, we expect that SPAM contributes to an overall reduction in the amplitude of the oscillations when benchmarked against the theoretical estimations in Fig. 2(d), an effect that was already observed in the Rabi experiments of Figs. 1(g) and 1(h).

Looking at the impact of gate imperfections, at $\theta = 0$, we naively may expect that neither single-qubit nor two-qubit operations change the initial state $|\downarrow\rangle^{\otimes N}$, since $X(0)$ is a microwave drive of duration $t_{\mathrm{MW}} = 0$, and the CNOT logic remains inactive when the qubits remain in $|\downarrow\rangle$. However, since the CNOT gates are compiled using a sequence of single-qubit rotations and free precession under the exchange interaction [Fig. 2(c)], we can expect that both gate errors and dephasing contribute to a reduction in visibility even at $\theta = 0$. Because the number of CNOT gates increases with system size, compounding errors could explain why the observed return probability at $\theta = 0$ drops with N.

When $\theta \neq n\pi$ with $n \in \mathbb{N}$, the operation $X(\theta)$ brings the qubits involved to a point in the Bloch sphere where they become susceptible to dephasing. An important observation is that when gates are implemented sequentially, as is the case here, dephasing effects quickly accumulate as the circuit depth increases due to the many idling qubits. In some cases, the idling times experienced by specific qubits become comparable to their T_2^* times, as seen in Fig. 3 and discussed further below. Additionally, the $X(\theta)$ rotations themselves introduce small errors, which result in a lower return probability for $\theta = 2\pi$ than for $\theta = 0$. This is aggravated by qubit dephasing following imperfect $X(2\pi)$ rotations and imperfect CNOTs.

Aimed at modeling the impact of dephasing, we quantify T_2^* using Ramsey-like experiments in Fig. 3(a). We note that spin relaxation is typically negligible compared to dephasing due to its timescale being orders of magnitude longer than those of interest ($\approx$ 100's ms). The dephasing rates have been shown to be contingent on whether the qubits are operated in isolation or with active exchange interaction J [16]. For this reason, we present T_2^* measurements on all qubits in the two-qubit subspace over a range of barrier voltages taking the coupling from "on" to "off." Dephasing is mostly caused by charge noise displacing the electrons in the micromagnet magnetic field gradient [36], as well as by residual ^{29}Si nuclear spins coupling through the hyperfine interaction. In the J_{on} regime, the qubit frequency additionally becomes sensitive to charge noise modulating the exchange interaction. Despite operating at the symmetry point (see Fig. S6 from Supplemental Material S7 [32]), where the impact of charge noise is expected to be minimized [37], we indeed observe a reduction in T_2^* times as J increases for all qubit pairs. Interestingly, the dephasing times for J_{off} remain close to the values measured over two years earlier on the same device [28], even though we now operate at 200 mK and multiple thermal cycles to room temperature have taken place.

We compare the measured T_2^* values to the idling times for each qubit as a function of varying system size N and circuit length $\theta = \{0, \pi/2, \pi, 2\pi\}$ (excluding initialization and readout) in Fig. 3(b). The idling periods are indicated by the yellow lines connecting the quantum gates in

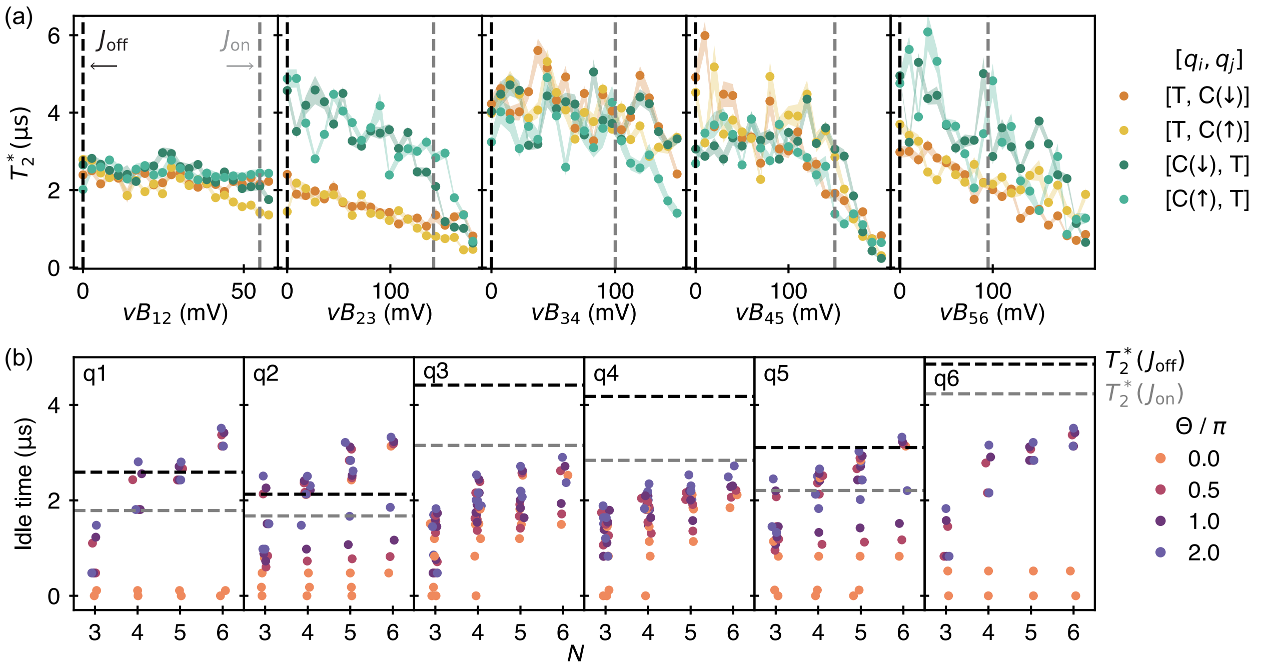

FIG. 3. Idling timescales and dephasing times. (a) T_2^* times extracted from Ramsey experiments for all six qubits, conditional on the state (↑ or ↓) of a neighboring qubit, and as a function of virtual barrier pulse amplitude vB_{ij}. Each panel shows the T_2^* values for the two qubits i and j adjacent to the virtual barrier gate vB_{ij}. The labels T and C refer to the target and control qubit, respectively, with the target qubit being the one measured. The vertical dashed lines mark the values of $vB_{\rm ij}$ at which single- ($J_{\rm off}$) and two-qubit ($J_{\rm on}$) operations are executed. (b) Total idle times experienced by individual qubits 1–6 throughout the circuit as a function of the number of qubits involved in the circuit N. For clarity, the modest amount of jitter has been added to the x-axis to separate the data points. As expected, idle times increase with N, as quantum logic is applied sequentially. Fewer data points are available for the edge qubits, due to a reduced number of possible combinations. For instance, qubit 3 can be involved in running the circuit for $N = 3$ using qubits 1, 2, 3; 3, 2, 1; 2, 3, 4; 4, 3, 2; 3, 4, 5 and 5, 4, 3; while qubit 1 can only be involved in circuits using qubits 1, 2, 3 and 3, 2, 1. The T_2^* values for the conditions $J_{\rm off}$ and $J_{\rm on}$ in (a) (averaged over the four sets of datapoints) are included as a visual guide to compare the decoherence times against the idling times, showing that the idle times are in many cases comparable to or even surpass T_2^*, in particular for qubits 1, 2 and 5.

Fig. 2(a). The horizontal dashed lines in Fig. 3(b) depict the T_2^* times obtained from Fig. 3(a) in the $J_{\rm off}$ and $J_{\rm on}$ regimes. Here, T_2^* in the $J_{\rm on}$ regime is the average T_2^* calculated across all possible interaction conditions. For example, for qubit 3, we take the mean value for the T_2^* obtained when qubit 2 is in either the $|{\downarrow}\rangle$ or $|{\uparrow}\rangle$ state, as well as when qubit 4 is in either the $|{\downarrow}\rangle$ or $|{\uparrow}\rangle$ state. Notably, for some qubits such as qubit 1, 2, and 5, the idling times in the circuit exceed their respective T_2^*.

Using the T_2^* measurements, we model the evolution of the N-qubit state in the presence of quasi-static phase noise during both idling times and quantum operations. The details can be found in Supplemental Sec. S8 [32], and the results are presented in Fig. 2(f). As in the experimental plots, we show the average behavior obtained when running the simulations for all possible qubit combinations, using actual gate durations and measured T_2^* times. While this model is not intended to quantitatively reproduce the measured data, it is sufficient to observe that pure dephasing competing with the operational speed can reproduce some of the trends present in the data, such as an N-dependent reduction in the visibility of the oscillations (including at $\theta = 0$) and a decay as a function of θ.

The Loschmidt echo amplitude only captures how dissimilar the evolved quantum state is from the initial state, offering no additional information about the time-evolved state itself. However, for specific qubit combinations (i.e., 2–3–4; 4–3–2; 3–4–5; 5–4–3; 2–3–4–5 and 5–4–3–2), it is also possible to access the value of the magnetization along the z axis, $M_z = 1/N \sum_{i=1}^{N} Z_i$, using the readout sequence of Fig. 1(a). Specifically, we can directly exctract a measure of Z for qubits 3 and 4 from $\mathcal{M}_{\rm QND}$ and for qubits 2 and 5 through $\mathcal{M}_{ZZ}^{\rm C}$, provided that neither qubits 1 and 6 are involved in the circuit. The magnetization along the z-axis is expected to behave as shown in Fig. 2(g), reaching zero at $\theta_{\rm c}$, which marks the point at which the state is anticipated to be maximally entangled. Figure 2(h) displays the experimentally obtained average magnetization for the accessible qubit combinations as a function of θ. In order to measure the reduced set of observables needed to extract the magnetization, we leave out the steps (CNOT+$\mathcal{M}_{ZZ}^{\rm D}$) from the readout sequence. Notably,

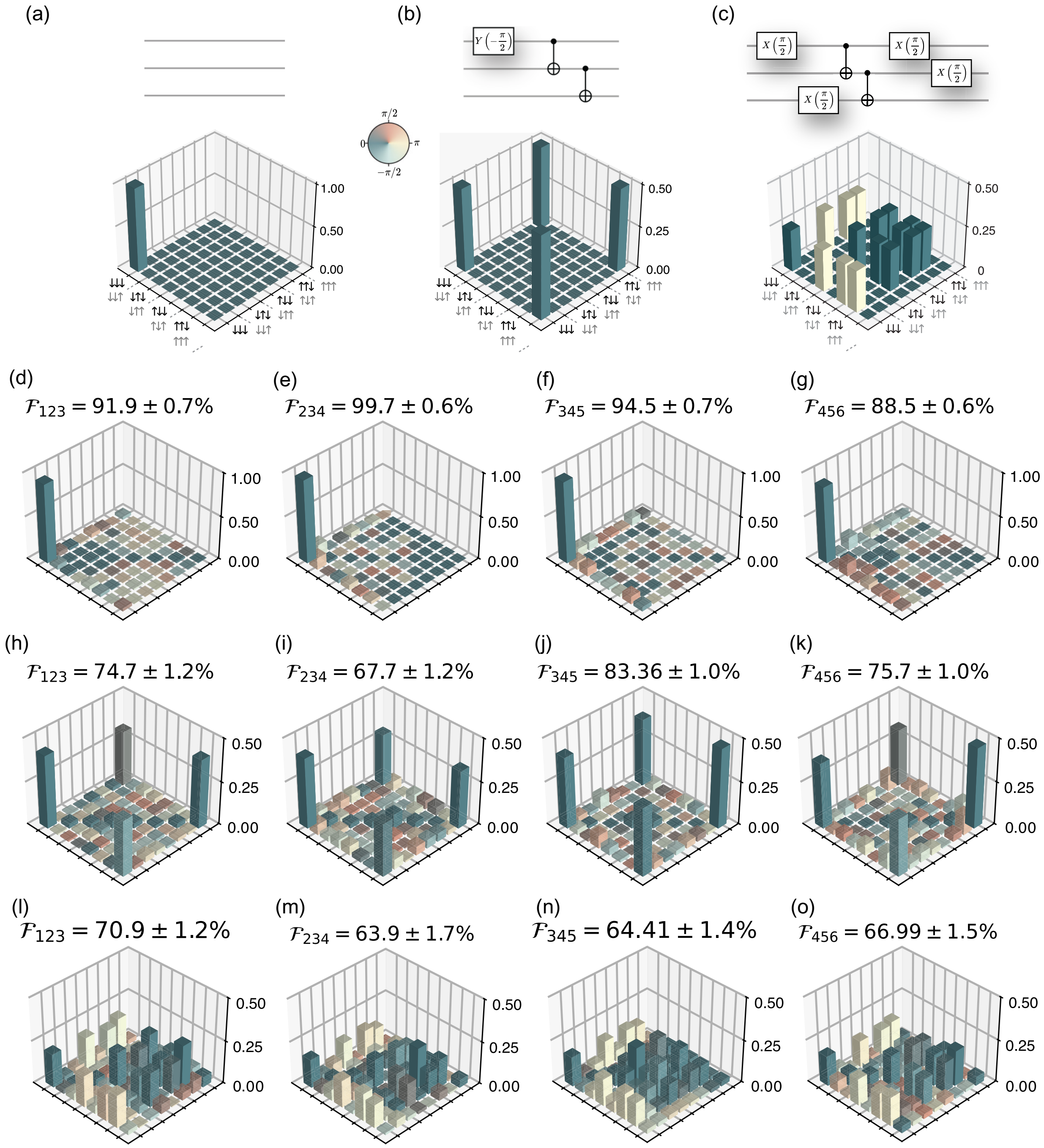

FIG. 4. Quantum state tomography for $N = 3$ at 200 mK. (a)–(c) Quantum circuits and expected density matrices for (a) the $|{\downarrow\downarrow\downarrow}\rangle$ state, (b) a GHZ state, and (c) the state obtained when executing the quantum circuit for $N = 3$ and $\theta = \pi/2$. The initialization and tomographic pulse sequence for state readout are omitted in the quantum circuits. (d)–(g) Experimentally measured density matrices for the circuit in (a), for four sets of three qubits ijk as indicated. The state fidelities $\mathcal{F}_{ijk}$ shown above each panel are calculated compensating for readout errors, and the error bars represent one standard deviation (1σ), calculated from 300 bootstrap resampling iterations. (h)–(k) Experimentally measured density matrices for the circuit in (b). The state fidelities for the GHZ states are calculated without loss of generality by considering the general form $|\psi_{\mathrm{GHZ}}\rangle = (|{\downarrow\downarrow\downarrow}\rangle + e^{i\phi}\,|{\uparrow\uparrow\uparrow}\rangle)/\sqrt{2}$ and fitting the arbitrary phase ϕ to maximize the fidelity. The analysis yields the modest values $\phi_{123} = -0.54$, $\phi_{234} = 0.16$, $\phi_{345} = 0.03$, $\phi_{456} = -0.54$. (l)–(o) Experimentally measured density matrices for the circuit in (c). The raw state fidelities without removal of readout errors are (b) 84.73%, (c) 87.08%, (d) 87.01%, (e) 87.87%, (g) 59.40%, (h) 47.89%, (i) 55.38%, (j) 57.71%, (l) 61.26%, (m) 47.90%, (n) 46.23%, and (o) 59.43%.

this contributes to a lower loss of visibility for Fig. 2(h) than seen in Fig. 2(e). We further compare the experimental results with numerical simulations which incorporate quasi-static dephasing noise shown in Fig. 2(i), which capture some of the deviations from the ideal result seen in experiments.

B. Quantum state tomography

The Loschmidt echo and magnetization are natural observables in the context of dynamical quantum phase transitions. As a means for assessing in detail how well the full system behaves under realistic workloads, we next perform full QST.

This gives insight, for instance, into the overall fidelity of the state at relevant points in the quantum circuit and into how well entanglement spreads across the array. We choose to examine three states, presented in Fig. 4; (a) the input state $|{\downarrow\downarrow\downarrow}\rangle$, (b) a three-qubit Greenberger-Horne-Zeilinger (GHZ) state for comparison, and (c) the final state when running the circuit in Fig. 2(a) for $N = 3$ and for the critical angle $\theta_c = \pi/2$, the angle θ that is expected to produce the strongest entanglement. The state $|\psi(\theta_c)\rangle$ is given by $\frac{1}{4}\left(|{\downarrow\downarrow\downarrow}\rangle + |{\downarrow\uparrow\uparrow}\rangle + |{\uparrow\downarrow\uparrow}\rangle + |{\uparrow\uparrow\downarrow}\rangle\right)$.

The set of operators used for the tomographic pulses is identical to those reported in [28], and we employ maximum likelihood estimation to obtain the density matrix ρ_{exp}. We limit the tomography to three and four qubits, as expanding the measurement space further is constrained by the coherence of the system. For example, the maximum duration of the pulse sequences required to construct the observables for tomography on four qubits already ranges from 830 to 1227 ns, depending on the specific qubits involved, with an average sequence duration of 560–745 ns. For five qubits, the range is 1347–1405 ns, with an average sequence length of 830–860 ns, while experiments for six qubits require pulse sequences up to 1922 ns long, with a mean of 1134 ns. These estimates only consider the duration of the gates used to construct the tomographic operators, excluding any additional time required for preparing the state of interest. Figure 4 displays the quantum state tomography results for various subsets of three qubits along the array (data for four qubits are presented in Supplemental Material S9 [32]). For reference, subfigures (a)–(c) depict the ideal target state for the respective quantum circuits. At the top of each panel showing experimental data, we indicate the state fidelities $\mathcal{F} = \langle\psi|\,\rho_{\mathrm{exp}}\,|\psi\rangle$ obtained after measurement error removal, with $|\psi\rangle$ being the ideally expected state. The results are consistent with state-of-the-art values reported for semiconductor qubit platforms [22,28]. We find that compared to previous work on this device [28], the unexpected arbitrary phases present in the off-diagonal elements of the density matrices for the GHZ states are largely absent. A similar improvement is seen in QST results on Bell States for all pairs of neighboring qubits (Supplemental Material S9 [32]). We explain this advance compared to earlier results in part by the fact that all the measurements were taken at 200 mK. This minimizes spurious phase accumulation due to microwave crosstalk and allows us to avoid prepulsing to saturate and thus stabilize the spin resonance frequencies before operation [29]. We also note that we observe variability in tomography fidelities across different qubit combinations, which depends on device tuning and measurement timing. In fact we observe similar trends reported in previous work on the same device at different operating temperatures [28]: for instance, a GHZ state on qubits 1–2–3 reached higher fidelity (76.8%) than those on 2–3–4 (71.4%) or 3–4–5 (72.2%), despite qubits 3–4–5 exhibiting longer coherence times and a shorter tomography sequence for 2–3–4. This illustrates that the relationship between state fidelity and single-qubit metrics is not straightforward. In line with this, our Bell-state tomography also shows lower fidelities for qubit pairs 2–3 and 3–4, suggesting that two-qubit gates are the dominant limiting factor. Finally, we illustrate the trend of state fidelity with system size in Fig. 5, which shows a summary plot of all state fidelities $\mathcal{F}$ reported in this manuscript as a function of the number of qubits N. Our results are consistent with the trend recently reported in Ref. [38] for donor-based spin qubits.

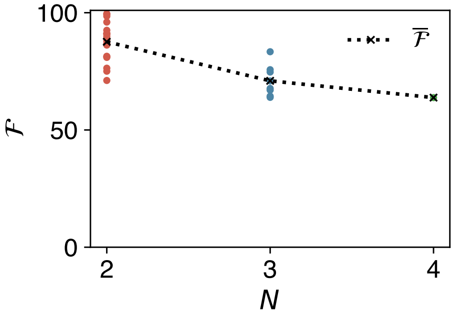

FIG. 5. Fidelity of entangled states as a function of qubit number N. Plotted are the state fidelities $\mathcal{F}$ obtained from quantum state tomography of the Bell states ($N = 2$), the state prepared by the circuit in Fig. 4(c) ($N = 3$), and GHZ states ($N = 3, 4$) in this work. A decrease in fidelity is observed as the number of qubits N increases. Colored dots represent the individual measurements, while black crosses denote the mean value.

V. DISCUSSION

In conclusion, we demonstrated the implementation of a realistic quantum circuit on a semiconductor spin-qubit device, utilizing a qubit register of up to six qubits—representing the largest quantum circuit executed in semiconductors to date. The circuit was inspired by a protocol designed to investigate dynamical quantum phase transitions in Ising-like systems. Its scaling features allowed us to benchmark the performance of our quantum processor as a function of system size N. By measuring the return probability and magnetization, we recover the expected periodic dynamics of the circuit, demonstrating that controlled interactions, enabled by sequentially activating neighboring couplings, can be achieved across the entire array. We find that the performance of the quantum processor is limited by dephasing, in particular for idling qubits, as well as by errors in state preparation and measurement. To assess the effects of dephasing, we experimentally measure T_2^* for each qubit and numerically simulate the time evolution of the system accounting for quasi-static phase noise both when idling and during single-qubit rotations. The numerical simulations qualitatively reproduce the main features observed in the experimental data, such as a reduction in visibility as a function of N as well as a degradation in the signal amplitude for longer evolution times. An additional overall reduction in the experimental visibility results from SPAM errors.

Unlike previous approaches that separately benchmark single- and two-qubit gates for individual qubits or qubit pairs or independently assess state preparation and measurement errors, the present implementation takes a more holistic approach. In all cases, we initialize and perform readout on all six qubits and execute qubit operations as a function of a variable parameter θ. This method enables us to evaluate the processor's capabilities comprehensively, without confining the analysis to specific quantum states or benchmarks and compare the results with simulations. We further characterize the overall system performance through quantum state tomography and highlight the importance of improving SPAM errors for better state estimation. We note that other benchmarks, such as quantum volume, could also be of benefit for these devices and would facilitate a direct comparison to different platforms. Our choice of a Loschmidt-echo–based protocol was motivated by its scaling behavior and by its connection to dynamical quantum phase transitions.

Future work should focus on mitigating dephasing effects from idling through the parallelization of single- [39,40] and two-qubit operations and possibly also by adopting new control strategies that achieve faster qubit operations, such as optimized baseband single-qubit control [41]. While dynamical decoupling could, in principle, extend coherence during idle periods, this would require simultaneous single-qubit operations to be practical, as well as sophisticated scheduling of the refocusing pulses in between the pulses that advance the computation. In addition, it will be important to enhance dephasing times, for instance through optimized nanomagnets that suppress decoherence gradients [42], and by reducing charge noise with improved dielectric gate stacks and using thinner quantum wells [36]. To further reduce hyperfine noise, isotopic purification should be improved compared to the current residual 800 ppm spinful nuclei and extended to the SiGe barrier above the quantum well.

ACKNOWLEDGMENTS

We acknowledge the contribution of A. Sammak to the development of the ^{28}Si/SiGe heterostructure. We thank M. Rimbach-Russ for input regarding the theoretical models, K. Capannelli for assistance with the data analysis rethresholding method and members of the Vandersypen groups for useful discussions. We acknowledge the anonymous reviewer for suggesting the inclusion of Fig. 5 in the new version of the manuscript. We thank P. Harvey-Collard for helpful suggestions regarding the rethresholding procedures. financial support from Intel, and the Army Research Office (ARO) under Grants No. W911NF-17-1-0274 and No. W911NF-12-1-0607. The views and conclusions contained in this document are those of the authors and should not be interpreted as representing the official policies, either expressed or implied, of the ARO or the U.S. Government. The U.S. Government is authorized to reproduce and distribute reprints for government purposes, notwithstanding any copyright notation herein. Development and maintenance of the growth facilities used for fabricating samples are supported by DOE (No. DE-FG02-03ER46028). We further acknowledge the financial support from the Dutch Ministry for Economic Affairs through the allowance for Topconsortia for Knowledge and Innovation (TKI) as well as support from the "Quantum Inspire–the Dutch Quantum Computer in the Cloud" project (Project No. NWA.1292.19.194) of the NWA research program "Research on Routes by Consortia (ORC)," funded by the Dutch Research Council (NWO).

DATA AVAILABILITY

The data that support the findings of this article are openly available [43].

APPENDIX: METHODS

1. Parity-mode Pauli Spin Blockade at the (3-1)–(4-0) charge configuration

Spin-to-charge conversion occurs at the (3,1)–(4,0) charge transition. In the (3,1) configuration, two electrons occupy the lowest energy valley state and one electron fills the next available valley orbital in the first dot, while the second dot contains one electron occupying the lowest valley state. Compared to the (1,1) occupation, this results in a larger energy gap to the next available orbital for the moving electron (from dot 2 or 5 in this case), thus increasing the readout window [28]. The Zeeman energy difference between qubits enables operation in the parity-mode regime, where the $|T_0\rangle$ state rapidly relaxes to the singlet state during the readout window, while the $|T_+\rangle$ and $|T_-\rangle$ states remain blockaded [30].

2. Zeeman energy differences and CZ gates

In the current settings, the Zeeman energy difference, ΔE_Z, between neighboring qubits is around 100's MHz, and exchange is operated in the few MHz regime. The comparatively large Zeeman energy difference suppresses the flip-flop terms in the exchange interaction, leading to a ZZ coupling Hamiltonian, which naturally realizes the CZ gate. An exception to this is qubits 3 and 4 which have a ΔE_Z of 10 MHz. However, adiabaticity in the switching of the J interaction ensures that the two-qubit operation is still a CZ gate [44].

3. Calibration routines

The measurement routines employed for the calibration of the device were the same as those discussed in detail in Fig. 4 of the extended data from the work of Philips *et al.* [28]. Here, operating at 200 mK allowed us to bypass the single-qubit phase crosstalk calibrations shown in subfigure (c), as crosstalk from microwave heating is mitigated. Crosstalk from direct off-resonant drive is reduced by ensuring that the qubit Larmor frequencies are well separated, with typical splittings of $\approx$ 100 MHz introduced by the micromagnet. An exception is qubits 3 and 4, whose separation is on the order of $\approx$ 10 MHz, depending on the specific tuning. In such cases, one can in principle exploit synchronization conditions [45], timing the Rabi frequencies so that the target qubit undergoes an integer π-rotation while an identity gate is effectively performed on the off-resonantly driven qubit. In our circuit, however, the rotation angle is varied continuously, which makes it difficult to satisfy this synchronization condition for all values of θ. Instead, we chose to work with modest Rabi frequencies of $\approx$ 1 MHz to suppress off-resonant driving. Lastly, for this cooldown, crosstalk arising from exchange-mediated ZZ interaction remains below 50 kHz for nearest-neighbor qubits.

4. Extracting broadening of the Loschmidt return probability

We quantify the broadening of the peaks as a function of N using the following procedure. For each experimental run (Fig. S5 [32]), we extract the maximum value of the Loschmidt echo amplitude near $\theta = 0$, denoted $\mathcal{L}^0_{\text{max}}$ and the minimum value near $\pi/2$, denoted $\mathcal{L}^{\pi/2}_{\text{min}}$. From these, we compute the midpoint $\mathcal{L}_{\text{mid}} = (\mathcal{L}^0_{\text{max}} + \mathcal{L}^{\pi/2}_{\text{min}})/2$ and determine the corresponding θ value $\theta^{<\pi/2}_{\text{mid}}$ by interpolation. Also using $\mathcal{L}_{\text{mid}}$, we similarly obtain $\theta^{>\pi/2}_{\text{mid}}$. From this, we obtain $\Delta\theta = \theta^{>\pi/2}_{\text{mid}} - \theta^{<\pi/2}_{\text{mid}}$, which serves as a measure of the width of the dip. Repeating this procedure for each trace allows us to build statistics across multiple realizations. The same analysis is applied to simulated data, both for the ideal case and for the case including quasistatic noise, enabling direct comparison between experiment and theory.

5. CNOT decomposition using the CZ gate

We leverage the native ZZ interaction to construct the CNOT operation, using the decomposition CNOT:= H CZ H, where H is the Hadamard gate and CZ := $Z_1(-\pi/2)Z_2(-\pi/2)U_{ZZ}(\pi\hbar/J)$, where U_{ZZ} is the unitary operator describing the ZZ interaction, $\hbar$ is the reduced Planck's constant and J is the value of the exchange interaction strength. The argument of the operator U_{ZZ} corresponds to the interaction time needed to obtain $CZ = \text{diag}(1, 1, 1, -1)$. In our implementation of the CNOT, the Hadamard gates are substituted by $Y(-\pi/2)$ and $Y(\pi/2)$. The equivalence is rooted in the fact that the Hadamard gate can be decomposed as $H = Y(-\pi/2)Z$ and $H = ZY(\pi/2)$. Since the Z gates commute with the CZ operation, they cancel out, resulting in the Y-based formulation.

[1] Google Quantum AI and Collaborators, Quantum error correction below the surface code threshold, Nature **638**, 920 (2025).

[2] D. Bluvstein, S. J. Evered, A. A. Geim, S. H. Li, H. Zhou, T. Manovitz, S. Ebadi, M. Cain, M. Kalinowski, D. Hangleiter *et al.*, Logical quantum processor based on reconfigurable atom arrays, Nature **626**, 58 (2024).

[3] M. DeCross, R. Haghshenas, M. Liu, E. Rinaldi, J. Gray, Y. Alexeev, C. H. Baldwin, J. P. Bartolotta, M. Bohn, E. Chertkov *et al.*, The computational power of random quantum circuits in arbitrary geometries, Phys. Rev. X **15**, 021052 (2025).

[4] A. Paetznick, M. da Silva, C. Ryan-Anderson, J. Bello-Rivas, J. Campora III, A. Chernoguzov, J. Dreiling, C. Foltz, F. Frachon, J. Gaebler *et al.*, Demonstration of logical qubits and repeated error correction with better-than-physical error rates, arXiv:2404.02280.

[5] S. Krinner, N. Lacroix, A. Remm, A. Di Paolo, E. Genois, C. Leroux, C. Hellings, S. Lazar, F. Swiadek, J. Herrmann *et al.*, Realizing repeated quantum error correction in a distance-three surface code, Nature **605**, 669 (2022).

[6] S. Ebadi, T. T. Wang, H. Levine, A. Keesling, G. Semeghini, A. Omran, D. Bluvstein, R. Samajdar, H. Pichler, W. W. Ho *et al.*, Quantum phases of matter on a 256-atom programmable quantum simulator, Nature **595**, 227 (2021).

[7] D. Bluvstein, A. Omran, H. Levine, A. Keesling, G. Semeghini, S. Ebadi, T. T. Wang, A. A. Michailidis, N. Maskara, W. W. Ho *et al.*, Controlling quantum many-body dynamics in driven Rydberg atom arrays, Science **371**, 1355 (2021).

[8] T. I. Andersen, N. Astrakhantsev, A. H. Karamlou, J. Berndtsson, J. Motruk, A. Szasz, J. A. Gross, A. Schuckert, T. Westerhout, Y. Zhang *et al.*, Thermalization and criticality on an analogue–digital quantum simulator, Nature **638**, 79 (2025).

[9] M. Gonzalez-Zalba, S. De Franceschi, E. Charbon, T. Meunier, M. Vinet, and A. Dzurak, Scaling silicon-based

quantum computing using CMOS technology, Nat. Electron. **4**, 872 (2021).

[10] A. Zwerver, T. Krähenmann, T. Watson, S. Bojarski, S. Amitonov, J. Boter *et al.*, Qubits made by advanced semiconductor manufacturing, Nat. Electron. **5**, 184 (2022).

[11] S. Neyens, O. K. Zietz, T. F. Watson, F. Luthi, A. Nethwewala, H. C. George, E. Henry, M. Islam, A. J. Wagner, F. Borjans *et al.*, Probing single electrons across 300-mm spin qubit wafers, Nature **629**, 80 (2024).

[12] A. Elsayed, M. Shehata, C. Godfrin, S. Kubicek, S. Massar, Y. Canvel, J. Jussot, G. Simion, M. Mongillo, D. Wan *et al.*, Low charge noise quantum dots with industrial CMOS manufacturing, Npj Quantum Inf. **10**, 70 (2024).

[13] H. C. George, M. T. Mądzik, E. M. Henry, A. J. Wagner, M. M. Islam, F. Borjans, E. J. Connors, J. Corrigan, M. Curry, M. K. Harper *et al.*, 12-spin-qubit arrays fabricated on a 300 mm semiconductor manufacturing line, Nano Lett. **25**, 793 (2024).

[14] S. D. Ha, E. Acuna, K. Raach, Z. T. Bloom, T. L. Brecht, J. M. Chappell, M. D. Choi, J. E. Christensen, I. T. Counts, D. Daprano *et al.*, Two-dimensional si spin qubit arrays with multilevel interconnects, PRX Quantum **6**, 030327 (2025).

[15] P. Steinacker, N. D. Stuyck, W. H. Lim, T. Tanttu, M. Feng, A. Nick, S. Serrano, M. Candido, J. D. Cifuentes, F. E. Hudson *et al.*, Industry-compatible silicon spin-qubit unit cells exceeding 99% fidelity, Nature (2025).

[16] X. Xue, M. Russ, N. Samkharadze, B. Undseth, A. Sammak, G. Scappucci, and L. M. Vandersypen, Quantum logic with spin qubits crossing the surface code threshold, Nature **601**, 343 (2022).

[17] A. Noiri, K. Takeda, T. Nakajima, T. Kobayashi, A. Sammak, G. Scappucci, and S. Tarucha, Fast universal quantum gate above the fault-tolerance threshold in silicon, Nature **601**, 338 (2022).

[18] T. Tanttu, W. H. Lim, J. Y. Huang, N. Dumoulin Stuyck, W. Gilbert, R. Y. Su, M. Feng, J. D. Cifuentes, A. E. Seedhouse, S. K. Seritan *et al.*, Assessment of the errors of high-fidelity two-qubit gates in silicon quantum dots, Nat. Phys. **20**, 1804 (2024).

[19] J. Y. Huang, R. Y. Su, W. H. Lim, M. Feng, B. van Straaten, B. Severin, W. Gilbert, N. Dumoulin Stuyck, T. Tanttu, S. Serrano *et al.*, High-fidelity spin qubit operation and algorithmic initialization above 1 K, Nature **627**, 772 (2024).

[20] K. Takeda, A. Noiri, T. Nakajima, L. C. Camenzind, T. Kobayashi, A. Sammak, G. Scappucci, and S. Tarucha, Rapid single-shot parity spin readout in a silicon double quantum dot with fidelity exceeding 99%, Npj Quantum Inf. **10**, 22 (2024).

[21] T. Watson, S. Philips, E. Kawakami, D. Ward, P. Scarlino, M. Veldhorst, D. Savage, M. Lagally, M. Friesen, S. Coppersmith *et al.*, A programmable two-qubit quantum processor in silicon, Nature **555**, 633 (2018).

[22] K. Takeda, A. Noiri, T. Nakajima, J. Yoneda, T. Kobayashi, and S. Tarucha, Quantum tomography of an entangled three-qubit state in silicon, Nat. Nanotechnol. **16**, 965 (2021).

[23] F. Van Riggelen, W. Lawrie, M. Russ, N. Hendrickx, A. Sammak, M. Rispler, B. Terhal, G. Scappucci, and M. Veldhorst, Phase flip code with semiconductor spin qubits, Npj Quantum Inf. **8**, 124 (2022).

[24] I. Thorvaldson, D. Poulos, C. M. Moehle, S. H. Misha, H. Edlbauer, J. Reiner, H. Geng, B. Voisin, M. T. Jones, M. B. Donnelly *et al.*, Grover's algorithm in a four-qubit silicon processor above the fault-tolerant threshold, Nat. Nanotechnol., 1 (2025).

[25] N. W. Hendrickx, W. I. Lawrie, M. Russ, F. van Riggelen, S. L. de Snoo, R. N. Schouten, A. Sammak, G. Scappucci, and M. Veldhorst, A four-qubit germanium quantum processor, Nature **591**, 580 (2021).

[26] X. Zhang, E. Morozova, M. Rimbach-Russ, D. Jirovec, T.-K. Hsiao, P. C. Fariña, C.-A. Wang, S. D. Oosterhout, A. Sammak, G. Scappucci *et al.*, Universal control of four singlet–triplet qubits, Nat. Nanotechnol. **20**, 209 (2025).

[27] V. John, C. X. Yu, B. van Straaten, E. A. Rodríguez-Mena, M. Rodríguez, S. Oosterhout, L. E. Stehouwer, G. Scappucci, M. Rimbach-Russ, S. Bosco *et al.*, Robust and localised control of a 10-spin qubit array in germanium, Nat. Commun. **16**, 10560 (2025).

[28] S. G. Philips, M. T. Madzik, S. V. Amitonov, S. L. de Snoo, M. Russ, N. Kalhor, C. Volk, W. I. Lawrie, D. Brousse, L. Tryputen *et al.*, Universal control of a six-qubit quantum processor in silicon, Nature **609**, 919 (2022).

[29] B. Undseth, O. Pietx-Casas, E. Raymenants, M. Mehmandoost, M. T. Madzik, S. G. Philips, S. L. De Snoo, D. J. Michalak, S. V. Amitonov, L. Tryputen *et al.*, Hotter is easier: Unexpected temperature dependence of spin qubit frequencies, Phys. Rev. X **13**, 041015 (2023).

[30] A. E. Seedhouse, T. Tanttu, R. C. Leon, R. Zhao, K. Y. Tan, B. Hensen, F. E. Hudson, K. M. Itoh, J. Yoneda, C. H. Yang *et al.*, Pauli blockade in silicon quantum dots with spin-orbit control, PRX Quantum **2**, 010303 (2021).

[31] T. Nakajima, A. Noiri, J. Yoneda, M. R. Delbecq, P. Stano, T. Otsuka, K. Takeda, S. Amaha, G. Allison, K. Kawasaki *et al.*, Quantum non-demolition measurement of an electron spin qubit, Nat. Nanotechnol. **14**, 555 (2019).

[32] See Supplemental Material: http://link.aps.org/supplemental/10.1103/f285-l2v5, which includes Refs. [46–54].

[33] P. Jurcevic, H. Shen, P. Hauke, C. Maier, T. Brydges, C. Hempel, B. P. Lanyon, M. Heyl, R. Blatt, and C. F. Roos, Direct observation of dynamical quantum phase transitions in an interacting many-body system, Phys. Rev. Lett. **119**, 080501 (2017).

[34] K. Xu, Z.-H. Sun, W. Liu, Y.-R. Zhang, H. Li, H. Dong, W. Ren, P. Zhang, F. Nori, D. Zheng *et al.*, Probing dynamical phase transitions with a superconducting quantum simulator, Sci. Adv. **6**, eaba4935 (2020).

[35] Y. Kim, C. J. Wood, T. J. Yoder, S. T. Merkel, J. M. Gambetta, K. Temme, and A. Kandala, Scalable error mitigation for noisy quantum circuits produces competitive expectation values, Nat. Phys. **19**, 752 (2023).

[36] B. Paquelet Wuetz, D. Degli Esposti, A.-M. J. Zwerver, S. V. Amitonov, M. Botifoll, J. Arbiol, A. Sammak, L. M. Vandersypen, M. Russ, and G. Scappucci, Reducing charge noise in quantum dots by using thin silicon quantum wells, Nat. Commun. **14**, 1385 (2023).

[37] M. Reed, B. Maune, R. Andrews, M. Borselli, K. Eng, M. Jura, A. Kiselev, T. Ladd, S. Merkel, I. Milosavljevic *et al.*, Reduced sensitivity to charge noise in semiconductor spin qubits via symmetric operation, Phys. Rev. Lett. **116**, 110402 (2016).

[38] H. Edlbauer, J. Wang, A. Huq, I. Thorvaldson, M. T. Jones, S. H. Misha, W. J. Pappas, C. M. Moehle, Y.-L. Hsueh, H. Bornemann *et al.*, An 11-qubit atom processor in silicon, arXiv:2506.03567.

[39] W. Lawrie, M. Rimbach-Russ, F. v. Riggelen, N. Hendrickx, S. d. Snoo, A. Sammak, G. Scappucci, J. Helsen, and M. Veldhorst, Simultaneous single-qubit driving of semiconductor spin qubits at the fault-tolerant threshold, Nat. Commun. **14**, 3617 (2023).

[40] Y.-H. Wu, L. C. Camenzind, P. Bütler, I. K. Jin, A. Noiri, K. Takeda, T. Nakajima, T. Kobayashi, G. Scappucci, H.-S. Goan *et al.*, Simultaneous high-fidelity single-qubit gates in a spin qubit array, arXiv:2507.11918.

[41] F. K. Unseld, B. Undseth, E. Raymenants, Y. Matsumoto, S. Karwal, O. Pietx-Casas, A. S. Ivlev, M. Meyer, A. Sammak, M. Veldhorst *et al.*, Baseband control of single-electron silicon spin qubits in two dimensions, Nat. Commun. **16**, 5606 (2025).

[42] M. Aldeghi, R. Allenspach, A. Vervelaki, D. Jetter, K. Bagani, F. Braakman, M. Poggio, and G. Salis, Simulation and measurement of stray fields for the manipulation of spin qubits in one-and two-dimensional arrays, Nano Lett. **25**, 1838 (2025).

[43] I. Fernández de Fuenes *et al.*, https://doi.org/10.5281/zenodo.15480419.

[44] M. Rimbach-Russ, S. G. Philips, X. Xue, and L. M. Vandersypen, Simple framework for systematic high-fidelity gate operations, Quantum Sci. Technol. **8**, 045025 (2023).

[45] I. Heinz and G. Burkard, Crosstalk analysis for single-qubit and two-qubit gates in spin qubit arrays, Phys. Rev. B **104**, 045420 (2021).

[46] Y. Y. Liu, S. G. J. Philips, L. A. Orona, N. Samkharadze, T. McJunkin, E. R. MacQuarrie, M. A. Eriksson, L. M. K. Vandersypen, and A. Yacoby, Radio-frequency reflectometry in silicon-based quantum dots, Phys. Rev. Appl. **16**, 014057 (2021).

[47] A. T. Schmitz, Thermal stability of dynamical phase transitions in higher dimensional stabilizer codes, arXiv:2002.11733.

[48] F. J. Wegner, Duality in generalized ising models and phase transitions without local order parameters, J. Math. Phys. **12**, 2259 (1971).

[49] V. Verteletskyi, T.-C. Yen, and A. F. Izmaylov, Measurement optimization in the variational quantum eigensolver using a minimum clique cover, J. Chem. Phys. **152**, 124114 (2020).

[50] P. Gokhale, O. Angiuli, Y. Ding, K. Gui, T. Tomesh, M. Suchara, M. Martonosi, and F. T. Chong, $o(n^3)$ measurement cost for variational quantum eigensolver on molecular hamiltonians, IEEE Trans. Quantum Eng. **1**, 1 (2020).

[51] O. Crawford, B. van Straaten, D. Wang, T. Parks, E. Campbell, and S. Brierley, Efficient quantum measurement of Pauli operators in the presence of finite sampling error, Quantum **5**, 385 (2021).

[52] A. T. Schmitz, M. Ibrahim, N. P. D. Sawaya, G. G. Guerreschi, J. Paykin, X.-C. Wu, and A. Y. Matsuura, in *2023 IEEE International Conference on Quantum Computing and Engineering (QCE)* (IEEE, Bellevue, Washington, USA, 2023), Vol. 01, p. 727.

[53] M. Heyl, Dynamical quantum phase transitions: A review, Rep. Prog. Phys. **81**, 054001 (2018).

[54] F. Martins, F. K. Malinowski, P. D. Nissen, E. Barnes, S. Fallahi, G. C. Gardner, M. J. Manfra, C. M. Marcus, and F. Kuemmeth, Noise suppression using symmetric exchange gates in spin qubits, Phys. Rev. Lett. **116**, 116801 (2016).